Scientia Iranica, Vol. 8, No. 2, pp 101–109
© Sharif University of Technology, April 2001

SCIENTIA
IRANICA

Wave Interaction and Acoustic Analysis in Liquid Rocket Engines

R. Ebrahimi[1], K. Mazaheri* and A. Ghafourian[1]

Wave interaction plays an essential part in analyzing the instability modes in rocket engines. While for low amplitude waves, the classic acoustic analysis is widely used, for high amplitude waves, physics of interaction and its effects on instability is still a major field of research. Combination of traveling and standing waves makes this task even harder. In this paper, different types of nonlinear waves are considered and, theoretically or numerically, their interactions are analyzed. Conditions under which wave deformation is negligible are presented. A method of mode identification is introduced based on linear advection of waves with preassumed shapes. To verify this method, results from previous studies in which modes were identified are used. This is especially important in mode identification after instability observation in experimental results of a rocket engine. Results indicate that nonlinear effects often have negligible influence on wave deformations in practical liquid rocket engines and the introduced method is capable of nonlinear wave analysis in this special situation.

INTRODUCTION

To obtain an effective procedure for design of liquid propellant rocket engines, control of combustion process is necessary. Combustion instability has remained one of the most critical problems in development of liquid propellant rocket engines. This phenomenon consists of a forced oscillation of combustion gases, driven by the combustion process, interacting with the resonance effects of the chamber geometry [1-4]. Oscillatory operation of a rocket engine is undesirable for many reasons.

Combustion instabilities may be regarded as the unsteady motion of a dynamic system capable of sustaining oscillations over a broad range of frequencies [5]. If the amplitude is small, the instability is closely related to classical acoustic behavior occurring in the absence of combustion and mean flow. Therefore, the geometry of the chamber has a dominant influence. Corresponding to classical results, traveling and standing waves are found [2,5,6], which are driven by the combustion process energy release and are influenced by the mean flow as well as the conditions at the injector face and exhaust.

Under suitable circumstances, the flow of energy to the waves may dominate the losses in such a way that nonlinear behavior becomes significant. In extreme cases, shock waves may form. The propagation speed of disturbances is a weak function of the amplitude, thus, the frequencies do not differ greatly from classical values computed for the same geometry.

There are three recognized types of combustion instability; low frequency instability (10-200 Hz), intermediate frequency instability (200-1000 Hz) and high frequency instability (greater than 1000 Hz), which includes excitation of acoustic vibrational modes of the combustion chamber and is, by far, the most destructive kind of instability and hardest to control [6,7].

In an actual engine with high frequency instability, several modes could be present simultaneously. These modes may correspond to the longitudinal, radial or tangential modes of the chamber and could be of traveling or standing nature. Pressure signal measurements from the chamber have been used to determine the modes [3,8,9]. Fast Fourier transform of pressure signals, which is commonly used for this

1. *Department of Aerospace Engineering, Sharif University of Technology, Tehran, I.R. Iran.*
*. *Corresponding Author, Department of Aerospace Engineering, Sharif University of Technology, Tehran, I.R. Iran.*

purpose, is not sufficient when standing steep waves are present; since it may overestimate the frequency of these waves by a factor of two as will be shown later. It also does not provide an insight into the physics of the instability modes. Using high speed photography and film recording, luminosity from a two dimensional transparent-wall combustion chamber has been used to determine the instability modes [3,10,11].

Here, first the interaction of several different finite amplitude waves are studied and using analytical and numerical tools, conditions are searched for under which nonlinearity of wave deformation is negligible. Then, it is shown that these conditions are often met in real liquid rocket engines. A simple linear method applicable for analysis of experimental measurements done for detection of combustion instability mode is presented. In this method, by reconstruction of measured pressure waves and their phase variation along the chamber, the instability modes can be identified. For this purpose, by presumption of the instability modes, the appropriate waves are produced numerically at each end of a combustion tube with appropriate amplitude and frequency. With these boundary conditions, the classical acoustic equations are solved. Experimentally produced amplitude and phase time histories are examined and compared with their presumed theoretical equivalents to identify the instability modes present.

In the following sections, numerical analysis of wave interaction, interaction of nonlinear waves, validity of the superposition assumption for nonlinear steep waves and application of the present method in mode identification are described.

NUMERICAL ANALYSIS OF WAVE INTERACTION

To attain classical wave equation, mass, momentum and energy equations are linearized for an inviscid, adiabatic, nonreactive and quiescent media. The following equation is obtained:

$$\nabla^2 p = \frac{1}{a^2}\frac{\partial^2 p}{\partial t^2}, \tag{1}$$

in which a is the speed of sound. This equation is written as a system of first-order equations:

$$\frac{\partial p}{\partial t} = \pm a \frac{\partial p}{\partial x}, \tag{2}$$

where + and − signs pertain to right- and left-traveling waves. For discretization of these equations, the first-order upwind scheme is used:

$$\frac{p_i^{n+1} - p_i^n}{\Delta t} = -\frac{a}{\Delta x}\left(p_i^n - p_{i-1}^n\right)$$

right traveling waves. (3)

For left traveling waves, a similar equation can be written. In the particular case of $c = \frac{a\Delta t}{\Delta x} = 1$, the numerical solution is the same as the exact solution of the wave equation.

Specific modes are generated in a combustion tube with both ends open. A left traveling wave with particular amplitude is generated continuously at the right end. The left end of the tube is assumed to act as an open end with respect to this left traveling wave. At the same time, a right traveling wave is continuously generated at the left end for which the right end is assumed to be open. Depending on the mode which is to be generated, different amplitudes and phases can be assigned to each of these imposed waves.

With these boundary conditions and using the above mentioned scheme, Equation 2 is solved. Pressure and phase history are computed along the tube for that particular mode. Application of this method for interaction of nonlinear waves is questionable, which is the subject of the following section.

INTERACTION OF NONLINEAR WAVES

In the combustion chamber of rockets, the chemical reaction of propellants gives high energy density to the compressible gases within the chamber. Combustion processes can couple with unsteady motion of gases. The flow of a small portion of the total combustion energy to the acoustic waves may dominate the losses such that nonlinear behavior becomes significant and shock waves may form. Under these conditions, validity of the results from classical wave equation has to be determined. It must be shown that while the formation of steep waves is nonlinear, their propagation and interaction are linear. To show this, interaction of two shock waves, two expansion waves and two steep fronted waves are analyzed in the following sections.

Interaction of Two Shock Waves

Consider two shock waves which are traveling toward each other through a quiescent media ($u_o = 0$), as shown in Figure 1. The propagation velocities of left and right traveling shock waves are C_{S1} and C_{S2}, respectively. The thermophysical properties of region (0) and pressure ratios of shock waves are known. The shock velocity C_{S1}, the mass motion velocity u_1 and the density and temperature ratios across the left traveling shock wave are calculated from the following

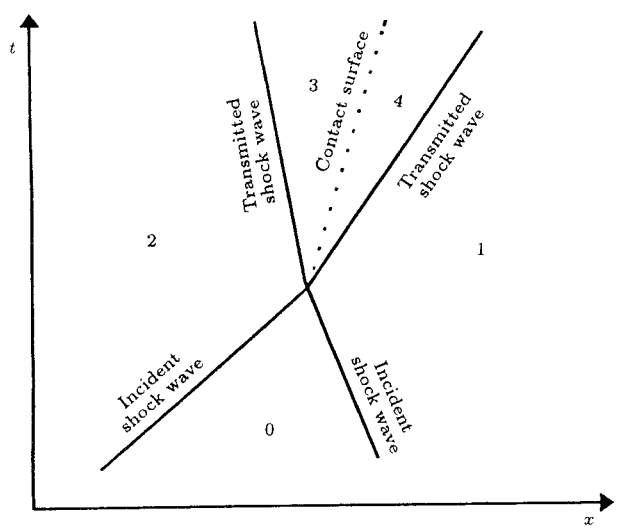

Figure 1. Interaction of two shock waves on an $x-t$ diagram.

equations [12]:

$$C_{S1} = a_o\sqrt{\frac{\gamma+1}{2\gamma}\left(\frac{p_1}{p_o}-1\right)+1}, \tag{4}$$

$$u_1 = \frac{a_o}{\gamma}\left(\frac{p_1}{p_o}-1\right)\left[\frac{\frac{2\gamma}{\gamma+1}}{\frac{p_1}{p_o}+\frac{\gamma-1}{\gamma+1}}\right]^{1/2}, \tag{5}$$

$$\frac{T_1}{T_o} = \frac{p_1}{p_o}\left[\frac{\frac{\gamma+1}{\gamma-1}+\frac{p_1}{p_o}}{1+\frac{\gamma+1}{\gamma-1}\left(\frac{p_1}{p_o}\right)}\right], \tag{6}$$

$$\frac{\rho_1}{\rho_o} = \frac{1+\frac{\gamma+1}{\gamma-1}\left(\frac{p_1}{p_o}\right)}{\frac{\gamma+1}{\gamma-1}+\frac{p_1}{p_0}}. \tag{7}$$

By replacing $\frac{p_2}{p_o}$ in the above equations, the same values are calculated for the right traveling shock wave.

After collision, four regions exist in the $x-t$ diagram. Regions 1 and 4 represent front and back of the right traveling wave, while Regions 2 and 3 represent the same values for the left traveling wave, respectively. The shock velocities of these waves are C_{S3} and C_{S4}. The pressure ratios of the traveling shock waves are different, therefore, there exists a contact surface between Regions 3 and 4. Across the contact surface, the entropy changes discontinuously, but pressure and velocity are continuous.

In order to calculate the properties of Region 4, continuity, momentum and energy equations are written between Regions 1 and 4. For simplicity, all velocities are measured with respect to the shock wave. Therefore, it is obtained that:

$$\rho_1(C_{S4}+u_1) = \rho_4(C_{S4}-u_4), \tag{8}$$

$$p_1+\rho_1(C_{S4}+u_1)^2 = p_4+\rho_4(C_{S4}-u_4)^2, \tag{9}$$

$$h_1+\frac{1}{2}(C_{S4}+u_1)^2 = h2+\frac{1}{2}(C_{S4}-u_4)^2. \tag{10}$$

After some manipulation, the shock and induced mass velocity of the right traveling wave are found as:

$$C_{S4} = a_1\sqrt{\frac{\gamma+1}{2\gamma}\left(\frac{p_4}{p_1}-1\right)+1}-u_1, \tag{11}$$

$$u_4 = \frac{a_1}{\gamma}\left(\frac{p_4}{p_1}-1\right)\left[\frac{\frac{2\gamma}{\gamma+1}}{\left(\frac{p_4}{p_1}\right)+\frac{\gamma-1}{\gamma+1}}\right]^{1/2}-u_1. \tag{12}$$

In the same manner, the values of C_{S3} and u_3 are calculated.

Recalling that $u_3 = u_4$ and $p_3 = p_4$, one can find:

$$\left\{-\frac{a_2}{\gamma}\left(\frac{p_3}{p_2}-1\right)\left[\frac{\frac{2\gamma}{\gamma+1}}{\left(\frac{p_3}{p_2}\right)+\frac{\gamma-1}{\gamma+1}}\right]^{1/2}+u_2\right\} - \left\{\frac{a_1}{\gamma}\left(\frac{p_3}{p_1}-1\right)\left[\frac{\frac{2\gamma}{\gamma+1}}{\left(\frac{p_3}{p_1}\right)+\frac{\gamma-1}{\gamma+1}}\right]^{1/2}-u_1\right\} = 0. \tag{13}$$

Since the properties of regions 1 and 2 are known, the value of p_3 can be calculated from the above equation by iterative means. Therefore, the values of C_{S4} and $u_3 = u_4$ are calculated from Equations 11 and 12. By replacing $\frac{p_1}{p_o}$ with $\frac{p_4}{p_1}$ and $\frac{p_3}{p_2}$ in Equations 6 and 7, the temperature and density of Regions 3 and 4 can be obtained, respectively.

Now, the influence of the nonlinearities on the shape deformation for two incident shock waves can be studied. For this purpose, a new parameter α defined as $\frac{(p_1-p_o)}{p_o}-\frac{(p_3-p_2)}{p_o}$ is introduced and the variation of α with respect to the strength of the shock waves $\left(\frac{p_1-p_o}{p_o}\right.$ and $\left.\frac{p_2-p_o}{p_o}\right)$ is calculated using the above equations. The contours of parameter α are presented in Figure 2. The behavior of this parameter when the strengths of left and right traveling shock waves are equal has been shown in Figure 3. As can be seen, when $\frac{p_1-p_o}{p_o}$ is less than 24.57%, the shape deformation of shock wave due to collision with another shock wave is less than 5%. Therefore, for condition of $\frac{p_1-p_o}{p_o}$ being less than 24.57%, the linear theory can be used for analysis of shock wave interaction.

Interaction of Two Expansion Waves

The interaction of two simple expansion waves traveling in opposite directions is illustrated in Figure 4. The

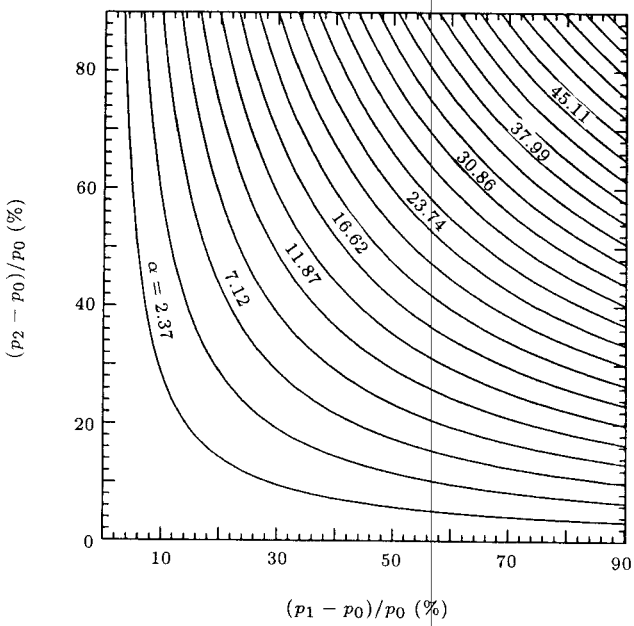

Figure 2. Variation of parameter α due to interaction of two shock waves with different strengths.

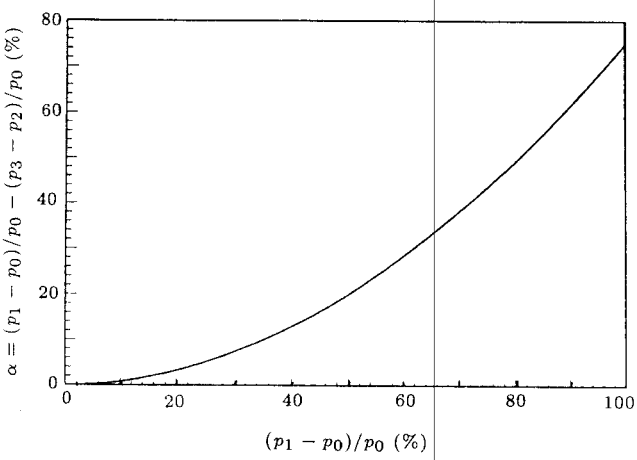

Figure 3. Variation of parameter α due to interaction of two shock waves with the same strength.

thermophysical properties of the quiescent Region 0 and pressure ratios of traveling expansion waves are known. J_+ Riemann invariant, i.e., $u + \frac{2a}{\gamma-1}$, is constant considering the left traveling simple expansion wave. Since the expansion wave is isentropic, $\rho_1 = \rho_o(p_1/p_o)^{1/\gamma}$, therefore, $a_1 = \sqrt{\frac{\gamma}{\rho_1}\left(\frac{p_1}{p_o}\right)p_o}$ and, it is found that:

$$u_1 = u_0 + \frac{2}{\gamma - 1}(a_0 - a_1). \tag{14}$$

Also, using the right traveling simple expansion wave, it is observed that J_- Riemann invariant is constant and u_2 is similarly calculated.

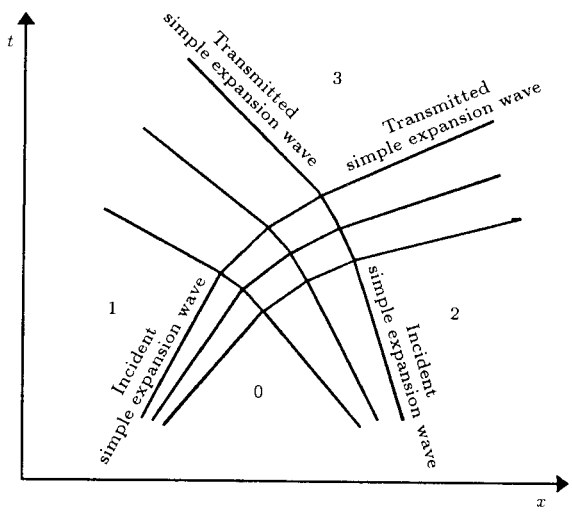

Figure 4. Interaction of two expansion waves on an $x - t$ diagram.

For transmitted simple expansion waves,

$$u_1 - \frac{2a_1}{\gamma - 1} = u_3 - \frac{2a_3}{\gamma - 1}$$

right traveling expansion wave, (15)

$$u_2 + \frac{2a_2}{\gamma - 1} = u_3 + \frac{2a_3}{\gamma - 1}$$

left traveling expansion wave. (16)

Adding Equations 15 and 16, one obtains u_3 and a_3. Since the flow is isentropic, the pressure ratio across the right traveling transmitted expansion wave is obtained as:

$$\frac{p_2}{p_3} = \left(\frac{\gamma R T_2}{a_3^2}\right)^{\gamma/(\gamma+1)}. \tag{17}$$

By replacing T_2 with T_1 in Equation 17, the pressure ratio of the left traveling transmitted expansion wave is found.

Now, the effects of nonlinearities on the shape deformation of an expansion wave after its collision with another expansion wave can be considered. Here, to observe this, a new parameter β defined as $\frac{(p_o - p_1)}{p_o} - \frac{(p_2 - p_3)}{p_o}$ is introduced and the variation of this parameter with respect to the strength of expansion waves $\left(\frac{p_o - p_1}{p_o}$ and $\frac{p_o - p_2}{p_o}\right)$ is calculated, the results of which are presented in Figure 5. The behavior of parameter β when the strengths of the two incident expansion waves are equal has been shown in Figure 6. As shown in this figure, when the strength of expansion wave $\frac{p_o - p_1}{p_o}$ is less than 23.69%, the effect of nonlinearities on the shape deformation of the incident expansion waves is less than 5%. Thus, the linear theory can be used for analysis of the expansion wave interaction when $\frac{p_o - p_1}{p_o}$ is less than 23.69%.

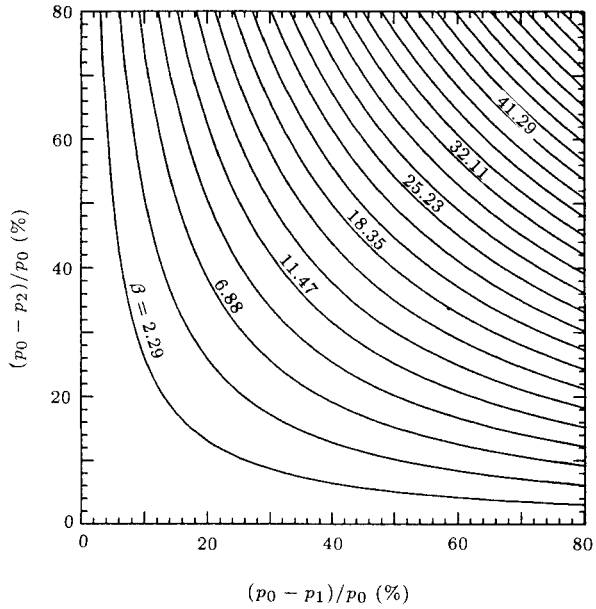

Figure 5. Variation of parameter β due to interaction of two expansion waves with different strengths.

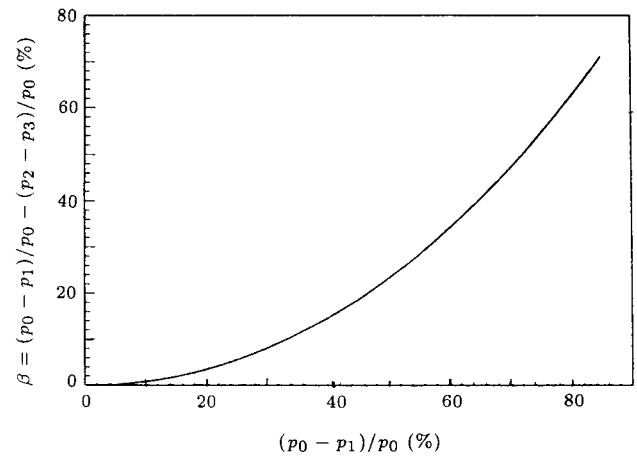

Figure 6. Variation of parameter β due to interaction of two expansion waves with the same strength.

Interaction of Two Steep Waves

Waves formed after a finite time from traveling of a harmonic wave with finite amplitude are considered as a steep wave, consisting of a shock wave followed by a gradually weakening expansion wave. The propagation and interaction of nonlinear steep waves are complicated and, therefore, studied only through numerical solution of nonlinear Euler equations. The variation of amplitude and area of a wave during interaction and collision with another wave are two parameters which are used to determine the influence of nonlinearity on the wave deformation. These parameters are computed for a wave during its propagation and are compared with parameters which are found for the same wave without any collision. If the difference of these parameters in the two cases is negligible, it is possible to assume that the superposition of nonlinear waves is valid for this particular application.

Numerical Solution of the Nonlinear Waves

The propagation and collision of nonlinear waves in a one dimensional tube are studied by solving Euler equations. The governing equations are:

$$\frac{\partial \mathbf{U}}{\partial t} + \frac{\partial \mathbf{F}}{\partial x} = 0, \tag{18}$$

where two vectors $\mathbf{U}$ and $\mathbf{F}$ are:

$$\mathbf{U} = \begin{pmatrix} \rho \\ \rho u \\ \rho E \end{pmatrix}, \quad \mathbf{F} = \begin{pmatrix} \rho u \\ \rho u^2 + p \\ \rho u H \end{pmatrix}. \tag{19}$$

For discretization on a numerical grid, Equation 4 is integrated over the i-th cell, to find:

$$\frac{\partial \mathbf{U}_i}{\partial t} = -\frac{1}{\Delta v_i} \sum_{sides} \left(\tilde{\mathbf{F}} \cdot S \right). \tag{20}$$

According to van Leer flux vector splitting [13], the flux vectors become:

$$F_1^{\pm} = \pm \frac{1}{4} \rho a (M \pm 1)^2 , \tag{21}$$

$$F_2^{\pm} = F_1^{\pm} \left(u - \frac{p}{\rho a^2} (u \mp 2a) \right) , \tag{22}$$

$$F_3^{\pm} = F_1^{\pm} \left(H - \frac{h/a^2}{1 + 2h/a^2} (u \mp a)^2 \right) . \tag{23}$$

MUSCL (Monotone Upstream-centred Schemes for Conservation Laws) method is used to increase the spatial order of accuracy [14]. In this method, primitive variables are defined as follows:

$$\tilde{\mathbf{U}}^{\mathbf{t}} = (\rho,\ u,\ p) . \tag{24}$$

The numerical flux vector on $i + \frac{1}{2}$ side is written as:

$$\tilde{\mathbf{F}}_{i+\frac{1}{2}} = \mathbf{F}^{+} \left(\tilde{\mathbf{U}}^{L}_{i+\frac{1}{2}} \right) + \mathbf{F}^{-} \left(\tilde{\mathbf{U}}^{R}_{i+\frac{1}{2}} \right) . \tag{25}$$

General forms of the primitive variable vectors $\tilde{\mathbf{U}}^{R}_{i+\frac{1}{2}}$ and $\tilde{\mathbf{U}}^{L}_{i+\frac{1}{2}}$, when including the Minmod flux limiter functions, are:

$$\tilde{\mathbf{U}}^{L}_{i+\frac{1}{2}} = \tilde{\mathbf{U}}_i + \frac{\theta}{4} \left((1-\kappa)\phi^{-} + (1+\kappa)\phi^{+} \right)_i , \tag{26}$$

$$\tilde{\mathbf{U}}^{R}_{i+\frac{1}{2}} = \tilde{\mathbf{U}}_{i+1} - \frac{\theta}{4} \left((1-\kappa)\phi^{+} + (1+\kappa)\phi^{-} \right)_{i+1} . \tag{27}$$

For $\theta = 1$ and $\kappa = \frac{1}{3}$, the third order upwind is achieved. More information on this method and the functions ϕ^{-} and ϕ^{+} can be found in [15].

Shape Deformation of Interacted Steep Waves

The coupling and mutual effects of high amplitude right and left traveling waves are studied through solving nonlinear Euler equations. The superposition hypothesis of nonlinear waves is confirmed, if the interaction of waves does not change the shape and amplitude of them after they have passed over each other.

Consider a one-dimensional pipe with both ends open and an initial pressure distribution of:

$$p=\begin{cases} p_o + p_- \sin\left[\frac{2\pi}{\lambda}(x - x_R)\right], & x_R \le x \le x_R + \frac{\lambda}{2} \\ p_o + p_+ \sin\left[\frac{2\pi}{\lambda}(x - x_L)\right], & x_L \le x \le x_L + \frac{\lambda}{2} \\ p_o & \text{elsewhere} \end{cases} \quad (28)$$

This initial pressure distribution includes two half sine waves at points x_R and x_L. The coefficients p_+ and p_- represent the amplitude of the right and left traveling waves, respectively, and p_o is the reference pressure. It is assumed that $p_+ = p_- = p^*$. In order to study the collision of these two waves, initial conditions of the other properties are calculated from Riemann invariants such that the waves positioned at x_R and x_L travel to left and right, respectively. Thus, initial conditions of the other properties are [12]:

$$\frac{u}{a_o} = \pm\frac{2}{\gamma - 1}\left[\left(\frac{p}{p_o}\right)^{\frac{\gamma-1}{2\gamma}} - 1\right], \quad (29)$$

$$\frac{T}{T_o} = \left[1 \pm \frac{\gamma - 1}{2}\left(\frac{u}{a_o}\right)\right]^2, \quad (30)$$

where + and − indicate the properties of the right and left traveling waves, respectively. Neumann boundary condition is assumed on both sides of the pipe. For small values of p^*, the shape of these waves does not change during traveling and collision. By increasing the value of p^*, the wave front speed increases such that the waves quickly transform into shock and expansion waves. For this condition, when the left traveling wave has passed the other wave and is positioned at a particular location, its amplitude and area under the curve are computed. Also, in the absence of the right traveling wave, the same values are calculated using the same method for the left traveling wave when it is at the same position.

The ratios of amplitude change $\frac{\delta p}{p^*}$ and area under the curve change $\frac{\delta A}{A^*}$ for the left traveling wave at the particular position for two different conditions mentioned above are determined. Since the distances traveled by the wave in both cases are the same, it is expected that the dissipation and dispersion of the numerical method is almost canceled in the mentioned ratios. The computation is done for different values of $\frac{p^*}{p_o}$. Figure 7 shows the behavior of $\frac{\delta p}{p^*}$ and $\frac{\delta A}{A^*}$ with respect to $\frac{p^*}{p_o}$. As can be seen, even when the amplitude of the sharp wave is 2.2 times the reference pressure, the ratio of amplitude change is only 1.6% and that of area is 0.85%. Therefore, the superposition hypothesis of nonlinear waves hold with good accuracy for conditions of $\frac{p^*}{p_o} < 2$. In experimental observations of liquid rocket engine instabilities conducted so far, the ratio $\frac{p^*}{p_o}$ is less than 1.75 [16]. Thus, it is concluded that classical acoustic theory can be used in the analysis of wave coupling in the liquid rocket engines.

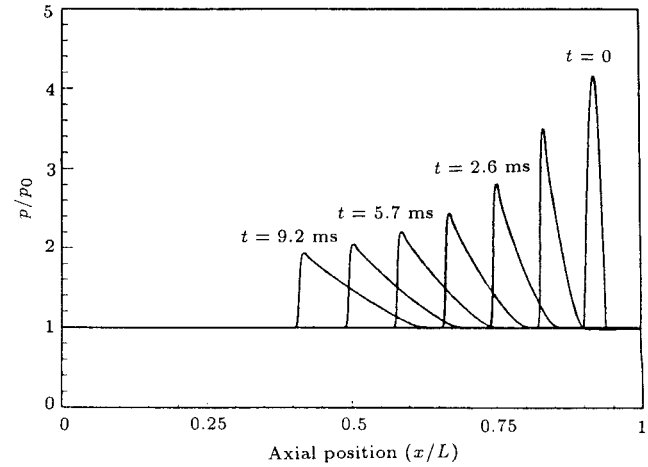

Figure 7. Shape deformation of a nonlinear wave due to interaction with another nonlinear wave with respect to strength of the wave.

APPLICATION AND RESULTS

To study different longitudinal modes in a pipe by the method of superposition of waves, at each end of the pipe, a periodic wave with particular amplitude and frequency is generated numerically. From the right end, left traveling wave and from the left end, right traveling wave are imposed.

Linear Waves

To generate the second longitudinal mode, harmonic waves with a same amplitude and wavelength equal to the length of the pipe are imposed on both sides of the pipe. The shape of the right and left traveling waves are:

$$p(t, \frac{x}{L} = 0) = f_L(t) = p_+ cos(\frac{2\pi t}{\tau}),$$

(right traveling wave), (31)

$$p(t, \frac{x}{L} = 1) = f_R(t) = p_- cos(\frac{2\pi t}{\tau}),$$

(left traveling wave), (32)

where p_+, p_- and τ are the amplitude of right and left traveling waves and period of oscillation, respectively.

For $p_- = 0$, only a right traveling wave exists in the pipe. The maximum and minimum pressures observed at different points in the pipe are constant and equal to $\pm p_+$. Phase difference of pressure variation with respect to time at different points in the pipe changes linearly with $\frac{x}{L}$. Since the wavelength is the same as the pipe length, the phase difference of pressure variation at the two ends is 360 degrees. If $p_- = p_+$, the second standing mode exists in the pipe. For this case, two complete antinodes are observed in the envelope of amplitude variations. The time variation of pressure at all points between nodes and antinodes are in the same phase and are 180 degrees out of phase with respect to the next node and antinode. In general, for the longitudinal standing modes, the number of nodes is equal to the order of the mode. For $0 < p_- < p_+$, the envelope of amplitude and phase variations are between the above two extreme cases.

Nonlinear Waves

The waves observed in liquid propellant rocket engines are mostly steep waves. The compression parts of harmonic waves due to nonlinear effects grow in amplitude as they propagate and become steep waves. To study this type of wave, two steep right and left traveling waves, with amplitudes such as $p_+ = p_- = p^*$ and wavelength equal to the pipe length, are generated at both ends of the pipe as shown in Figure 8a. These waves are the sharpened form of the second longitudinal mode. Since at the moment of the wave entrance from the right end, the wave propagating from the left also exists, the amplitude becomes $2p^*$, which is true for the left end wave as well.

From the solution of classical acoustic equation with the above given boundary conditions, it is observed that unlike the standing second longitudinal mode where two nodes existed at locations $\frac{x}{L} = 0.25$ and 0.75, there is no node at these points for the steep waves. The time variation of pressure at these points indicates the presence of waves with a frequency twice that of the frequency of the entering waves and amplitude of p^*. It can be seen that the time variation of pressure at the mid point of the pipe is the same as that of the entering waves. At intervals $0 < \frac{x}{L} < 0.25$, $0.25 < \frac{x}{L} < 0.75$ and $0.75 < \frac{x}{L} < 1$, the time variation of pressure has two peaks. One peak corresponds to the right traveling wave and the other to the left traveling wave as shown in Figures 8b and 8c. As points $\frac{x}{L} = 0.25$ and 0.75 are approached, the distance of these peaks increases and finally their shapes become the same. The phase variation with respect to $\frac{x}{L}$ is also studied. Unlike the phase variation of second standing harmonic wave which has a stepwise shape, for the steepened case, a diamond shape is observed. Phase curve varies linearly with respect to $\frac{x}{L}$, which is similar to the phase curve for consecutive impingement and

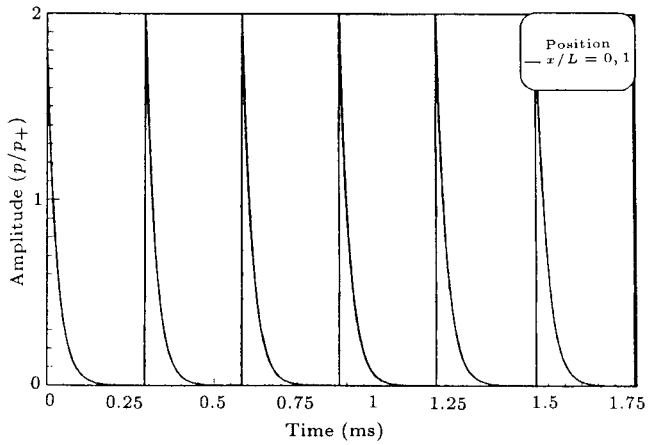

(a) Time variation of pressure at $^x/_L = 0, 1$

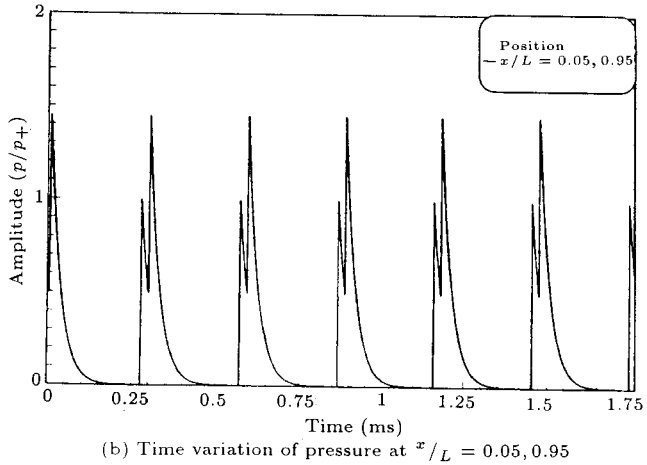

(b) Time variation of pressure at $^x/_L = 0.05, 0.95$

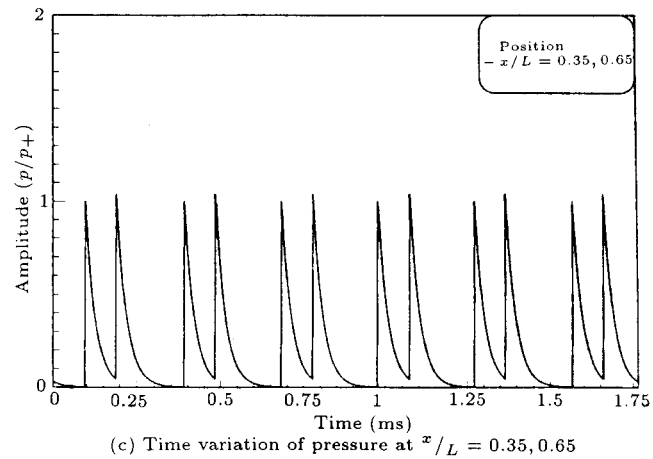

(c) Time variation of pressure at $^x/_L = 0.35, 0.65$

Figure 8. Time variation of pressure and phase diagrams for the second steep longitudinal wave in a pipe.

reflection of longitudinal waves to the walls of a closed cavity.

Next, a case is considered in which several modes exist in the combustion chamber at the same time [3]. Such a condition can be observed during long operations of engines or during transition from one mode to another mode. Figure 9a illustrates the time variation of pressure at point $\frac{x}{L} = 0.9$. The

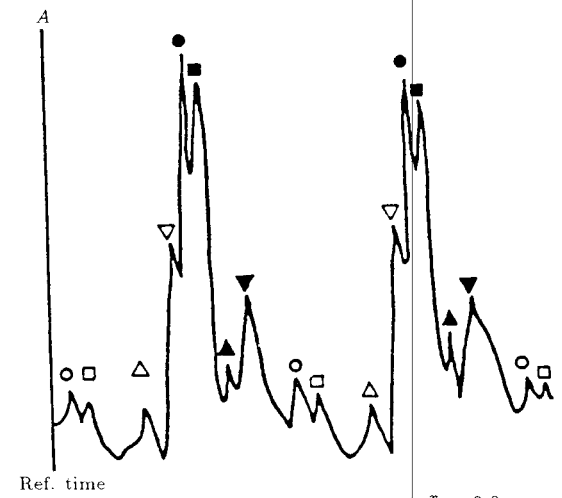

(a) Time variation of pressure at $\frac{x}{L} = 0.9$

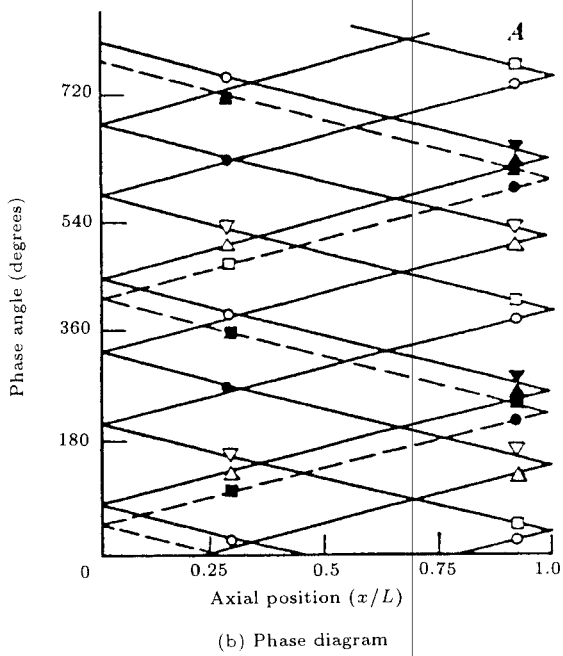

(b) Phase diagram

Figure 9. Pressure variation and phase diagrams for co-existing first and third steep longitudinal instabilities.

oscillations which are repeated continuously in this curve have eight peaks. Part (b) of Figure 9 shows the phase variation of pressure waves measured at different points of the engine. The dotted and continuous lines represent the first traveling and third standing modes, respectively. Since waves measured in the chamber are steep, the phase variation curve has a diamond shape. In order to generate the first mode numerically, waves with wavelength of twice the pipe length are imposed at the two ends of the pipe, having one period phase difference with respect to each other. For the third mode, the wavelength of the imposed waves is $\frac{2}{3}$ of the pipe length and their phase difference is half of their period.

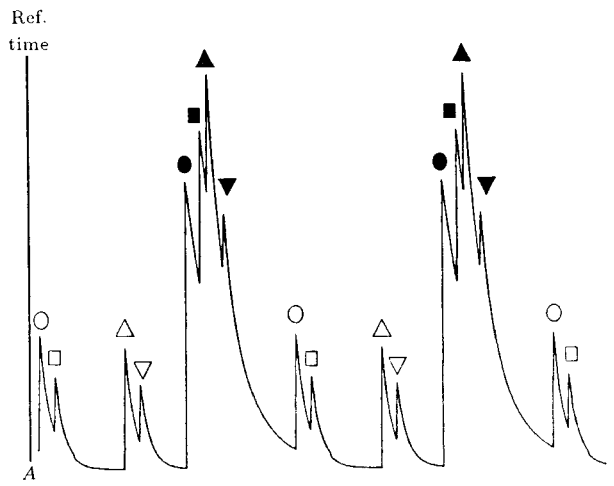

Figure 10. Computed pressure variation at $\frac{x}{L} = 0.9$ for co-existing first and third steep longitudinal instabilities.

The solution to acoustic equation with the above boundary conditions provides the time variation of pressure at point $\frac{x}{L} = 0.9$, as shown in Figure 10. The phase curve compares very well with the results of previous work [3]. For the pressure variation at point $\frac{x}{L} = 0.9$, eight consecutive peaks are observed which are repeated continuously. The amplitude of the oscillations do not match very well. However, the results of the numerical solution of acoustic equations can be used for the identification of acoustic modes in a chamber. This method becomes complicated when interaction of higher order modes exists and other complimentary methods should be used.

CONCLUSION

Single measurement of pressure using a high response pressure transducer is sufficient to indicate the existence of combustion instability in rocket engines. Regardless of the diagnostic tools, exact determination of instability modes and identification along with classification, as traveling, standing, spinning and precessing forms, require reconstruction of the waves through numerical means. This work presents a relatively simple tool for recognition and identification of various harmonic and steep waves existing in the combustion chamber. According to the computation and comparisons presented, the principle of superposition can be employed for all types of nonlinear waves observed in combustion chambers. Thus, at least in simple situations, if nonlinear waves are observed in pressure measurements, this method can be used to identify the nonlinear modes.

ACKNOWLEDGMENT

This project was funded by the defense industries organization. The authors wish to acknowledge the

support of the respective research management that made this study possible. The authors also extend their appreciation to the research deputy of Sharif University of Technology for the provided support.

NOMENCLATURE

a	velocity of sound, m/s
H	enthalpy, kJ/kg
t	time, s
C	wave velocity
i	cell index
$\mathbf{U}$	vector of conservative variables
c	Courant number
J	Riemann invarient
$\widetilde{\mathbf{U}}$	vector of primitive variables
E	total internal energy, kJ/kg
L	tube length, m
u	velocity, m/s
F	components of flux vector
M	Mach number, u/a
v	volume, m^3
$\mathbf{F}$	flux vector
p	pressure, Pa
x	axial position, m
$\widetilde{\mathbf{F}}$	numerical flux vector
S	cell face area, m^2
H	total enthalpy, kJ/kg
T	temperature, K

Greek Letters

α	shock wave deformation parameter
κ	parameter in Equations 12 and 13
β	expansion wave deformation parameter
λ	wavelength, m
γ	specific heat ratio
ρ	density, kg/m^3
Δ	difference
τ	wave period, s
θ	parameter in Equations 12 and 13
ϕ	flux limiter vector

Subscript and Superscript

L	left side
$+$	right traveling wave
o	reference values
$-$	left traveling wave
R	right side
$*$	amplitude of pressure oscillation
S	shock

REFERENCES

1. Crocco, L. and Harrje, D.T. "Combustion instability in liquid propellant rocket motors", *Experimental Method in Combustion Research (AGARD)* (1963).
2. Weiss, R.R. "An introduction to combustion instability in liquid propellant rocket engines", AFRPL-TR-66-150 (July 1966).
3. Harrje, D.T. and Reardon, F.H. "Liquid propellant rocket combustion instability", NASA SP-194 (1972).
4. Crocco, L. "Theoretical studies on liquid propellant rocket instability", *Tenth Symposium (International) on Combustion*, pp 1101-1128 (1965).
5. Culick, F.E. "Combustion instability in liquid-fueled propulsion system - An overview", AGARD-CP-450 (1989).
6. Reardon, F.H., Crocco, L. and Harrje, D.T. "Velocity effects in transverse mode liquid propellant rocket combustion instability", *AIAA Journal*, **2**(9) (Sept. 1964).
7. Crocco, L., Grey, J. and Harrje, D.T. "Theory of liquid propellant rocket combustion instability and its experimental verification", *ARS Journal* (Feb. 1960).
8. Ken, H.Y., Trouve, A. and Daily, J.W. "Low frequency pressure oscillations in a model ramjet combustor", *Journal of Fluid Mechanic*, **232**, pp 47-72 (1991).
9. Akbari, P. "Experimental investigation of combustion instability in a model ramjet", M.Sc. Thesis, Sharif University of Tehnology, Iran (1998).
10. Lawhead, R.B. "Photographic studies of combustion processes in liquid propellant rockets", *Eighth Symposium (International) on Combustion*, pp 1140-1151 (1963).
11. Levine, R.S. "Experimental status of high frequency liquid rocket combustion instability", *Tenth Symposium (International) on Combustion*, pp 1083-1099 (1965).
12. Landau, L.D. and Lifshitz, E.M. "Fluid mechanics", *Course of Theoretical Physics*, 2nd Ed., Pergamon Press **6**, pp 394-397 (1987).
13. Van Leer, B. "Flux vector splitting for the Euler equations", *Proc. 8th International Conference on Numerical Methods in Fluid Dynamics*, Berlin: Springer Verlag (1982).
14. Hirsch, C., *Numerical Computation of Internal and External Flows*, **2**, John Wiley & Sons, pp 494-505 (1990).
15. Yee, H.C. "A class of high resolution explicit and implicit shock capturing methods", NASA TM-101088, NASA AMES Research Center (Feb. 1989).
16. Barrere, M., et al., *Rocket Propulsion*, Van Nostrand Company, pp 689-691 (1959).